Materials Advances

ROYAL SOCIETY OF CHEMISTRY

PAPER

Published on 10 September 2026
Licensed under CC-BY 4.0

Check for updates

Cite this: *Mater. Adv.*, 2026, 7, 10217

Amino-functionalized metal organic framework fillers for stable all-solid-state lithium metal batteries

Sihao Xing, [ab] Gen Hasegawa, †[a] Prince Sharma, [a] Marcela Calpa, [a] Kyosuke Matsushita,[a] Denis Y. W. Yu, [a] Takuya Masuda, [ab] Kazunori Takada [a] and Naoaki Kuwata *[ab]

All-solid-state lithium metal batteries (ASSLBs) have attracted extensive attention due to their high safety and energy density. Poly(ethylene oxide) (PEO) is considered a promising solid polymer electrolyte owing to its excellent flexibility and processability. However, its practical application is hindered by the limited ionic conductivity, low Li-ion transference number, and unstable electrode/electrolyte interfaces. Herein, two structurally analogous metal organic framework (MOF) fillers with highly similar structures, with (MOF–NH_2) and without (MOF) amino functional groups, are introduced into a PEO-based electrolyte to elucidate the role of amino functionalization in regulating ion transport and interfacial chemistry. Density functional theory calculations reveal that compared with MOF and PEO, MOF–NH_2 exhibits the strongest interaction energy toward bis(trifluoromethanesulfonyl)imide ($TFSI^-$), facilitating LiTFSI dissociation and enhancing Li-ion transport. The strong interaction between amino groups and $TFSI^-$ effectively regulates anion distribution and interfacial reactivity, promoting the formation of LiF-rich interphases during electrochemical cycling. X-ray photoelectron spectroscopy and time-of-flight secondary ion mass spectrometry analyses reveal substantial LiF enrichment in both the solid electrolyte interphase and cathode electrolyte interphase, contributing to improved interfacial stability. As a result, with the addition of MOF–NH_2, the composite polymer electrolyte achieves an improved Li-ion transference number (0.29) and ionic conductivity (4.7×10^{-4} S cm^{-1}) at 60 °C. Besides, the optimized electrolyte enables stable lithium plating/stripping behavior and enhanced electrochemical performance. The Li/MOF–NH_2 + PEO/$LiFePO_4$ cell delivers a high-capacity retention of 90.5% after 550 cycles at 1 C at 60 °C. This work highlights the critical role of functional-group engineering in MOF fillers for manipulating anion chemistry, interphase formation, and ion transport, providing an effective strategy for the development of high-performance solid polymer electrolytes.

Received 27th July 2026,
Accepted 9th September 2026

DOI: 10.1039/d6ma01112h

rsc.li/materials-advances

1 Introduction

Lithium (Li) metal anodes, featuring an ultrahigh theoretical specific capacity and a low redox potential, are widely regarded as one of the most promising candidates for next-generation Li batteries.[1–3] However, when coupled with conventional liquid electrolytes, Li metal typically suffers from uncontrolled dendritic growth, which can lead to internal short circuits and severe safety hazards such as thermal runaway. To address these challenges and enable safer Li metal batteries, replacing liquid electrolytes with solid-state electrolytes (SSEs) has been proposed as an effective strategy.[4–6]

Among various SSEs, polymer-based electrolytes have emerged as strong candidates owing to their facile processability and mechanical flexibility.[7–10] In particular, poly(ethylene oxide) (PEO) has attracted extensive attention due to its excellent compatibility with Li metal, high salt solubility, film-forming ability, and flexibility.[11–15] Nevertheless, the practical application of PEO-based electrolytes remains hindered by limited ionic conductivity (σ), low Li-ion transference number (t_{Li^+}), and insufficient interfacial stability.[16–21]

To overcome these limitations, various strategies have been explored to enhance the performances of PEO-based electrolytes, including copolymerization, plasticization, and the

[a] *Center for Green Research on Energy and Environmental Materials, National Institute for Materials Science (NIMS), Tsukuba, Ibaraki 305-0044, Japan. E-mail: kuwata.naoaki@nims.go.jp*

[b] *Graduate School of Chemical Sciences and Engineering, Hokkaido University, Sapporo, Hokkaido 060-8628, Japan*

† Present address: Institute for Molecular Science (IMS), National Institutes of Natural Sciences (NINS), 38 Myodaiji, Okazaki, Aichi 444-8585, Japan. E-mail: gen-hasegawa@ims.ac.jp.

© 2026 The Author(s). Published by the Royal Society of Chemistry

incorporation of inorganic fillers.[22–25] Among these approaches, introducing inorganic fillers has been demonstrated to be an effective method for improving the electrochemical performances of PEO-based electrolytes. Representative examples include Al_2O_3, SiO_2, LLZO, $BaTiO_3$, g-C_3N_4, MXene and cellulose-based fillers.[26–34]

In addition to bulk modification, interfacial instability remains a critical issue. In particular, the interfacial reactions involving $TFSI^-$ play a critical role in determining the composition and stability of both the solid electrolyte interphase (SEI) and cathode electrolyte interphase (CEI).[35–38] Among the various interphase components, LiF is widely recognized as a desirable inorganic species because of its excellent chemical stability, mechanical robustness, and ability to suppress parasitic side reactions.[35] Therefore, regulating the coordination environment, distribution, and interfacial reactivity of $TFSI^-$ represents an attractive strategy for constructing stable electrode/electrolyte interphases and improving battery performance.[39,40]

Macromolecular frameworks with spatially extended structures, combined with functional groups, have been shown to effectively perturb molecular configurations and lower reaction energy barriers.[41,42] Among these materials, metal organic frameworks (MOFs) have attracted significant interest due to their abundant active sites and structural tunability.[43] Amino groups ($-NH_2$), possessing moderate electronegativity and strong polarity, can interact strongly with $TFSI^-$ through electrostatic interactions.[44] However, the influence of amino-functionalized fillers on $TFSI^-$ chemistry and the resulting interphase formation in PEO-based electrolytes remains insufficiently understood.

In this work, two structurally analogous MOF-based fillers, $[Cu_2(bza)_4(2\text{-apyr})]$ (MOF–NH_2; bza = benzoate, 2-apyr = 2-aminopyrimidine) and $[Cu_2(bza)_4(pyr)]$ (MOF; pyr = pyrimidine), were introduced into PEO polymer electrolyte to form two composite polymer electrolytes (CPEs). Unlike two-dimensional or three-dimensional MOFs, which are widely used as fillers for polymer electrolytes, both materials exhibit one-dimensional chain-like structures resembling the linear polymer backbone of PEO. This structural similarity may allow a more uniform distribution of fillers in CPEs. Both MOFs contain electron-deficient pyrimidine rings, which can generate electrostatic interactions with $TFSI^-$, so it is expected that their introduction can improve the performance of PEO electrolyte.[45] More importantly, these two MOFs differ mainly in the presence or absence of the $-NH_2$ functionality on the pyrimidine ring. The additional $-NH_2$ in MOF–NH_2 is expected to further strengthen the interaction with $TFSI^-$ through electrostatic interactions, providing an ideal model system for elucidating the role of $-NH_2$ functionalization. Density functional theory (DFT) calculations show that $TFSI^-$ interacts more strongly on MOF–NH_2 than MOF and PEO, thereby promoting the dissociation of Li salt, obtaining a higher concentration of free Li-ion (Li^+), and enhancing Li^+ transport. Previous studies have shown that the interaction between the filler and $TFSI^-$ can promote the formation of LiF-rich films.[35,46] In this study, X-ray photoelectron spectroscopy (XPS) and time-of-flight secondary ion mass spectrometry (TOF-SIMS) results demonstrated that MOF–NH_2 effectively regulates interphase chemistry, leading to the formation of LiF-rich SEI and CEI layers. As a result, Li–Li symmetric cells incorporating CPE with MOF–NH_2 exhibit stable cycling for over 1700 h at 0.1 mA cm^{-2} and 0.1 mAh cm^{-2}, while Li–$LiFePO_4$ (LFP) full cells deliver excellent cycling stability with a capacity retention of 90.5% after 550 cycles at 1 C at 60 °C. This work shows that the presence of amino functional groups on MOF fillers plays a decisive role in governing anion coordination, interfacial chemistry, and Li^+ transport, offering a practical design principle for next-generation high-performance CPEs.

2 Experimental section

2.1. Materials preparation

Poly(ethylene oxide) (PEO, Mw = 600 000 g mol^{-1}) was purchased from Sigma-Aldrich. Lithium bis(trifluoromethanesulfonyl)imide (LiTFSI, 99.99%), acetonitrile (>99.5%), $Cu(CH_3COO)_2{\cdot}H_2O$ (>95.0%), methanol (>99.8%), benzoic acid (>98.0%), ethyl acetate (>99.5%), *N*-methylpyrrolidone (NMP, >99.0%), 2-aminopyrimidine (2-apyr, >98.0%), 1,2-dimethoxyethane (DME, >99.0%) and pyrimidine (pyr, >98.0%) were purchased from Tokyo Chemical Industry Co., Ltd. $LiFePO_4$ powder, conductive carbon black (Super P), and poly(vinylidene fluoride) (PVDF 5130) binder were purchased from MTI Corporation. All chemicals were used without further purification. Li metals were purchased from HONJO metal corporation.

2.2. Synthesis of MOF and MOF–NH_2

MOF and MOF–NH_2 were prepared by a direct mixture method.[47,48] $Cu(CH_3COO)_2{\cdot}H_2O$ (1 mmol) and benzoic acid (2 mmol) were dissolved in a mixed solvent containing 40 mL of methanol and 40 mL of ethyl acetate under stirring at room temperature (500 rpm) for 3 h. Subsequently, 2-apyr (0.5 mmol) or pyr (0.5 mmol) was added directly as a solid (without prior dissolution) to the mixed solution and further stirred for 2 h. The resulting turbid suspension was collected by vacuum filtration, and the obtained powders were dried in air at room temperature overnight. The final products made with 2-apyr and pyr were $Cu_2(bza)_4(2\text{-apyr})$ and $Cu_2(bza)_4(pyr)$, respectively, denoted as MOF–NH_2 and MOF (isolated yields of 63% and 46%, respectively).

2.3. Preparation of composite polymer electrolytes

CPEs were prepared using a solution-casting method. First, MOF–NH_2 fillers (1–6 wt%, relative to the total solid content) or MOF filler (2 wt%) were dispersed in acetonitrile (16 mL) and sonicated for 10 min. Subsequently, anhydrous PEO (1.0 g) and LiTFSI (0.36 g) were added to the suspension with a fixed ether oxygen (EO)/Li molar ratio of 18 : 1, followed by magnetic stirring for 48 h to obtain homogeneous slurries. The resulting slurries were cast onto Teflon molds (7 cm × 7 cm) and air-dried for 6 h in ambient laboratory air to allow solvent evaporation. The obtained membranes were subsequently dried at 60 °C for 24 h under vacuum (oil-sealed rotary vane pump) to remove residual solvent and then transferred to an

© 2026 The Author(s). Published by the Royal Society of Chemistry

Ar-filled glovebox for storage and further use. For comparison, a filler-free electrolyte was prepared using the same procedure and denoted as PEO. The electrolytes containing MOF–NH_2 and MOF fillers were denoted as MOF–NH_2 + PEO and MOF + PEO, respectively.

2.4. Assembly of Li–Li symmetric coin cells

Li–Li symmetric cells were assembled in CR2032 coin cells using two Li metal foils and the prepared electrolyte membranes inside an Ar-filled glovebox (H_2O < 1 ppm, O_2 < 1 ppm). The diameters of the Li metal anodes and electrolyte membranes were 16 and 19 mm, respectively.

2.5. Preparation of $LiFePO_4$ cathodes and assembly of Li–LFP coin cells

The LFP cathode was prepared using LFP active material, conductive carbon black, and PVDF 5130 binder with a mass ratio of 8 : 1 : 1. The mixture was dispersed in NMP under stirring to form a homogeneous slurry. The slurry was coated onto an aluminum foil and dried overnight at 180 °C under vacuum. Finally, the electrode sheets were pressed using a roller press to ensure a strong bond between the current collector and the cathode material. The resulting electrodes were punched into circular disks with a diameter of 12 mm. The average active material loading was approximately 1–2 mg cm^{-2} and the typical electrode density was about 1 g cm^{-3}. Li–LFP coin cells were assembled in CR2032 coin cells using Li metal as the anode, the prepared electrolyte membrane, and the LFP cathode inside an Ar-filled glovebox (H_2O < 1 ppm, O_2 < 1 ppm). The diameters of the Li metal anode and electrolyte membrane were 16 and 19 mm, respectively. Galvanostatic charge/discharge measurements were conducted using a NEWARE battery testing system. Unless otherwise specified, the cells were cycled within a voltage range of 2.5–3.8 V. For $LiFePO_4$ cathodes, 1 C was defined as 170 mA g^{-1} based on the theoretical specific capacity of $LiFePO_4$ (170 mAh g^{-1}).

2.6. Materials characterizations

The crystal structures of the synthesized materials were characterized by X-ray diffraction (XRD, MiniFlex600, Rigaku, Japan). Fourier-transform infrared spectroscopy (FTIR, Nicolet iS50, Thermo Scientific, USA), Raman spectroscopy (RamanTouch-VIS-NIR, Nanophoton, Japan), and nuclear magnetic resonance (NMR, JNM-ECA400, JEOL, Japan) were employed to investigate the chemical structures and ion coordination environments of electrolyte membranes. Differential scanning calorimetry (DSC, Discovery DSC250Auto, TA Instruments, Japan) was performed to determine the glass transition temperature (T_g) and melting temperature (T_m) of the electrolyte membranes, with samples heated from −40 to 100 °C at a rate of 5 °C min^{-1} under an N_2 atmosphere. The chemical compositions of the cycled electrodes were analysed by XPS (VersaProbe II, ULVAC-PHI, Japan) and TOF-SIMS (TOF. SIMS5-AD-GCIB, IONTOF, Münster). The surface morphology of cycled Li anodes, fillers and electrolyte membranes was observed by scanning electron microscopy (SEM, JSM-7800F, JEOL, Japan) with energy dispersive spectroscopy (EDS). The mechanical properties of electrolyte membranes were evaluated by nanoindentation (iNano, KLA Corporation, USA). To prevent contamination during sample transfer, all air-sensitive samples were transferred using an air-tight transfer vessel without exposure to ambient atmosphere.

2.7. Electrochemical measurements

The ionic conductivity of the electrolyte membranes was evaluated by electrochemical impedance spectroscopy (EIS) using a high-frequency impedance system (4990EDMS-120K, TOYO, Japan). The measurements were conducted over a temperature range of 30–60 °C with a voltage amplitude of 10 mV and a frequency range of 1 MHz to 0.01 Hz. The electrolyte membrane was sandwiched between two stainless-steel blocking electrodes in CR2032 coin cell. After EIS testing, the cells were disassembled and the thickness of each compressed membrane was measured and used for σ calculations according to eqn (1):

$$\sigma = \frac{L}{R \times S} \tag{1}$$

where R is the bulk resistance of the electrolyte, L is the thickness of the electrolyte membrane (cm), and S is the contact area of the electrolyte and the stainless-steel electrodes (2.01 cm^2). Due to the inherent flexibility of the polymer electrolytes, it is difficult to ensure uniform thickness across all electrolytes. However, when assembling coin cells for conductivity measurements, we used spacers and spring plates of the same thickness and size, along with an automated coin cell assembly machine, which significantly reduced the influence of factors other than the thickness of the electrolyte itself.

To further investigate the temperature-dependent ionic conductivity behavior and elucidate the underlying ion transport mechanism, the conductivity data were analyzed using the Vogel–Tammann–Fulcher (VTF) eqn (2):

$$\sigma = A \cdot T^{-\frac{1}{2}} \exp\left(-\frac{B}{T - T_0}\right) \tag{2}$$

where A, B, and T_0 are VTF parameters for a given electrolyte. A is related to the pre-exponential factor associated with the effective concentration of mobile charge carriers, and B is related to the pseudo-activation energy of conductivity (E_a), which is calculated as $E_a = RB$, where R is the universal gas constant. T_0 (Vogel temperature) is set as 50 °C lower than the T_g measured by DSC.

The t_{Li^+} was measured using Li–Li symmetric cells under direct current (DC) polarization at 60 °C. A constant potential difference of 10 mV (ΔV) was applied, and the EIS spectra before and after polarization were collected in the frequency range of 1 MHz to 0.01 Hz. Polarization was continued until a steady-state current was reached. The t_{Li^+} was calculated according to eqn (3):

$$t_{Li^+} = \frac{I_s(\Delta V - I_0 R_0)}{(\Delta V - I_s R_s)} \tag{3}$$

where I_0 and I_s are the initial and steady-state currents, respectively, ΔV is the applied polarization voltage (10 mV), and R_0

© 2026 The Author(s). Published by the Royal Society of Chemistry

and R_s represent the initial and steady-state interfacial resistances, respectively.

The electrochemical stability window was determined using linear sweep voltammetry (LSV). The test was conducted using a CR2032 coin cell with a stainless-steel sheet as the working electrode and a Li metal as the counter electrode, sandwiched with an electrolyte membrane. The voltage range was from 0 to 6 V with a scan rate of 5 mV s^{-1}.

2.8. Density functional theory calculations

Density functional theory (DFT) calculations were performed using the GAMESS-US package to investigate the interactions between $TFSI^-$ and different materials.[49] Cluster models extracted from the corresponding frameworks were employed for the calculations. Initial interaction configurations were constructed based on the predicted interaction sites and subsequently optimized. All geometry optimizations and energy calculations were carried out in the gas phase using the B3LYP exchange–correlation functional with the 6-31G(d) basis set. The default numerical integration grid implemented in GAMESS-US was adopted, consisting of 96 radial points and 302 angular points. The self-consistent field energy convergence criterion was set to 0.0004 Hartree. For the electronic structure calculations, MOF, MOF–NH_2, PEO, and LiTFSI were treated as neutral singlet systems (charge = 0, multiplicity = 1), whereas $TFSI^-$ and the corresponding interaction complexes were assigned a charge of −1 and a multiplicity of 1. The interaction energy (E_{int}) was calculated according to eqn (4):

$$E_{int} = \sum E_{mol} - E_{total} \quad (4)$$

where E_{total} is the total energy of the optimized interaction complex and E_{mol} represents the energy of each isolated component.

3. Results and discussion

Fig. 1 illustrates the crystal structures of the two MOF-based fillers. The primary structural difference between MOF and MOF–NH_2 is the presence of –NH_2 on the organic ligand in MOF–NH_2. The SEM and EDS images of the two fillers are shown in Fig. S1. Both MOF and MOF–NH_2 exhibit elongated rod-like morphologies. EDS elemental mapping confirms the presence of C, N, O, and Cu in both materials, and all elements are uniformly distributed on the particles. The successful synthesis of MOF and MOF–NH_2 was confirmed by powder X-ray diffraction (PXRD). The powder samples were mechanically ground thoroughly before PXRD was performed. As shown in Fig. 2a, the PXRD patterns are in good agreement with the simulated ones, indicating the formation of the desired crystalline structures.[47,48] FTIR spectra (Fig. 2b) revealed the differences in their chemical composition. A broad absorption band at 3150–3530 cm^{-1} corresponding to N–H stretching vibrations is observed only for MOF–NH_2, and this difference can be attributed to –NH_2. FTIR of the three electrolyte membranes was performed. As shown in Fig. 2c, the characteristic N–H vibration remains detectable in MOF–NH_2 + PEO, indicating that the amino functionality is retained after incorporation into the PEO membrane. The morphology and elemental distribution of the PEO and CPEs were further analysed by SEM–EDS (Fig. S2). The EDS spectra of MOF + PEO and MOF–NH_2 + PEO showed uniform Cu element distributions, indicating that the filler was uniformly added to the PEO membrane. The influence of fillers on the ionic conductivity of polymer electrolytes is multifaceted, and changes in polymer dynamics are also an important factor. To assess whether incorporation of the fillers alters the crystallinity or thermal transition behavior of the PEO electrolyte, PXRD and DSC measurements were performed on the three electrolyte films. The PXRD patterns of PEO, MOF + PEO, and MOF–NH_2 + PEO exhibited comparable diffraction peak intensities corresponding to PEO, indicating that the crystallinity of the PEO electrolyte was only slightly affected by filler incorporation. The shifted features observed in the CPEs are attributed to the characteristic diffraction peaks of the MOF and MOF–NH_2 fillers themselves (Fig. S3a). DSC analysis showed that the three electrolytes exhibited nearly identical glass transition temperatures (T_g = −33.0, −33.1, and −32.4 °C for PEO, MOF + PEO, and MOF–NH_2 + PEO, respectively) and melting temperatures (T_m = 59.6, 59.3, and 59.0 °C, respectively) (Fig. S3b), further indicating that the incorporation of MOF and MOF–NH_2 fillers has only a limited influence on the segmental mobility and crystallinity of the PEO electrolyte.

The competitive coordination environment in the electrolyte and the dissociation of Li salts are critical factors governing Li^+

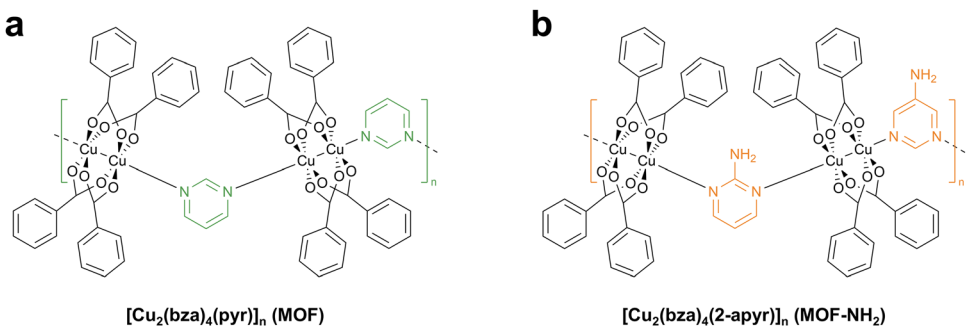


Fig. 1 The chemical structure of (a) MOF filler and (b) MOF–NH_2 filler.

© 2026 The Author(s). Published by the Royal Society of Chemistry

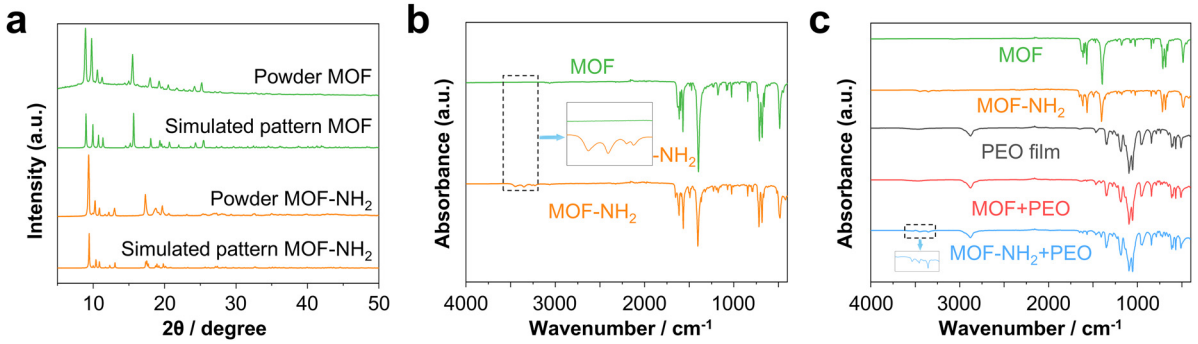


Fig. 2 (a) XRD patterns of MOF–NH_2 powder, MOF powder and simulated patterns of MOF–NH_2 and MOF. (b) FTIR spectra of MOF powder and MOF–NH_2 powder. (c) FTIR spectra of MOF powder, MOF–NH_2 powder, PEO film, MOF + PEO film and MOF–NH_2 + PEO film.

transport. Fig. 3a shows the FTIR spectra of the two CPEs and PEO from 1080 to 1000 cm^{-1}. The characteristic band located at ~1055 cm^{-1} is assigned to the coordinated EO segments of PEO. Upon incorporation of fillers, this band exhibits a noticeable blue shift, indicating strengthened interactions between EO segments and Li^+. This shift suggests an increased coordination of Li^+ with the polymer chains in the presence of fillers, especially with MOF–NH_2. Such behavior implies that

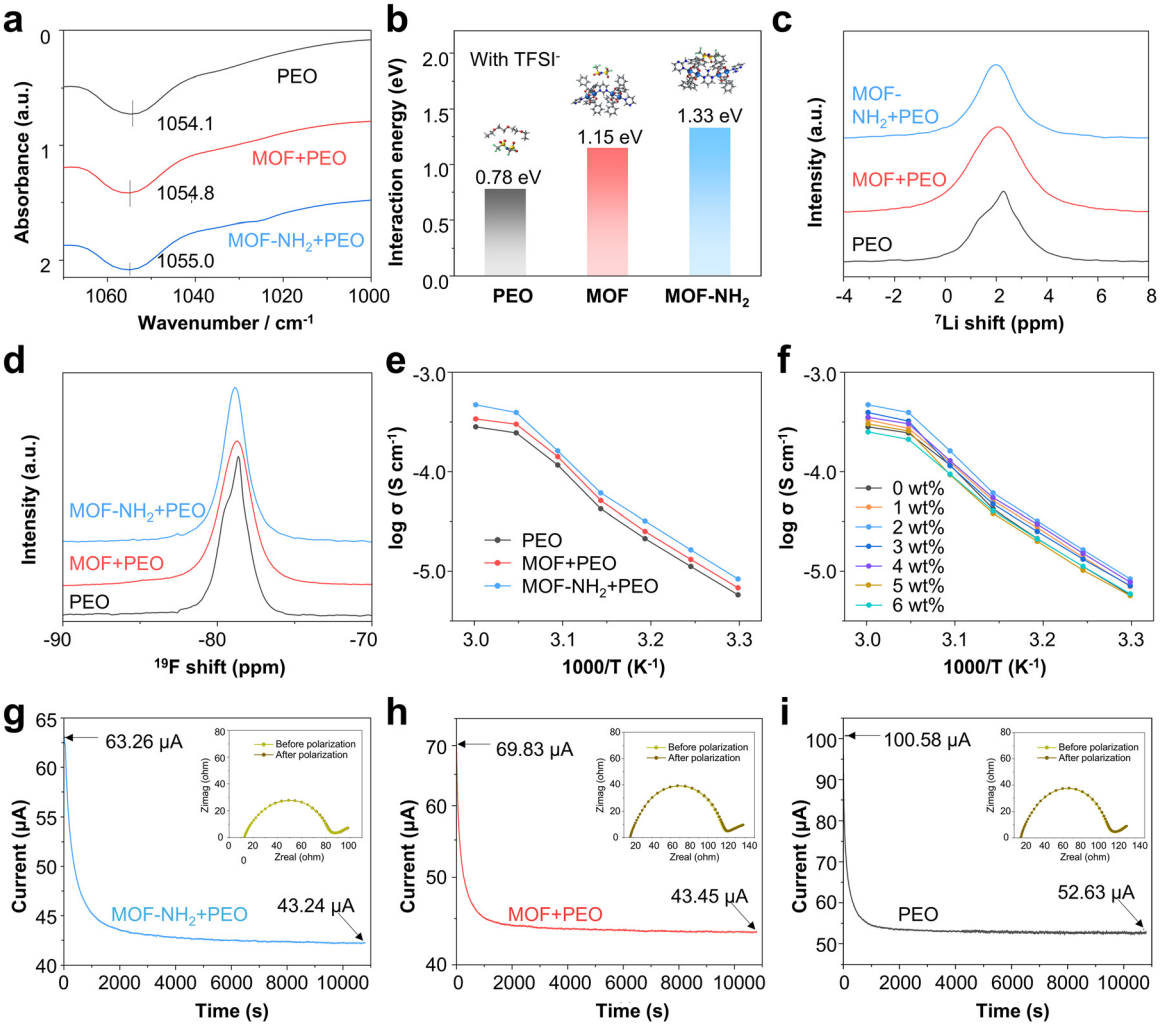


Fig. 3 (a) FTIR spectra of PEO, MOF + PEO, MOF–NH_2 + PEO, 1080–1000 cm^{-1}. (b) DFT calculation of interaction energy of PEO, MOF and MOF–NH_2 with $TFSI^-$. (c) and (d) ^7Li and ^{19}F NMR spectra of MOF–NH_2 + PEO and PEO from 30–60 °C respectively. (e) σ of PEO, MOF + PEO and MOF–NH_2 + PEO. (f) σ of 0, 1, 2, 3, 4, 5 and 6 wt% MOF–NH_2 + PEO. (g)–(i) t_{Li^+} testing of MOF–NH_2 + PEO, MOF + PEO and PEO respectively.

© 2026 The Author(s). Published by the Royal Society of Chemistry

the highly polar MOF–NH_2 filler introduces stronger interactions with LiTFSI, thereby promoting salt dissociation within the PEO electrolyte. To further quantify this effect, DFT calculations were performed to evaluate the interaction energies between different electrolyte components and $TFSI^-$. As shown in Fig. 3b, the calculated interaction energy between PEO and $TFSI^-$ is 0.78 eV, whereas the interaction energy between MOF and $TFSI^-$ increases to 1.15 eV, indicating a stronger interaction between the MOF and $TFSI^-$. This enhanced interaction may originate from electrostatic interaction between the electron-deficient pyrimidine rings in the MOF and $TFSI^-$.[45] The stronger interaction of $TFSI^-$ is expected to promote the dissociation of LiTFSI, thereby increasing the concentration of free Li^+ in the polymer electrolyte. Notably, MOF–NH_2 exhibits an even higher interaction energy toward $TFSI^-$ of 1.33 eV, indicating a significantly stronger interaction with $TFSI^-$. Since the primary structural difference between MOF and MOF–NH_2 is the presence of the –NH_2, the increased interaction energy suggests that the amino functionality further strengthens the interaction with $TFSI^-$. Such enhanced anion interaction is expected to facilitate LiTFSI dissociation and thereby alter the local ionic coordination structure within the polymer electrolyte. It should be noted that the differences in the interaction energies obtained from the DFT calculations are relatively small. Nevertheless, we believe that the observed trend in interaction energies provides some theoretical support for this interpretation. To verify this hypothesis, Raman spectroscopy was employed to investigate the coordination states of $TFSI^-$ (Fig. S4). The characteristic bands at 741 and 750 cm^{-1} correspond to Li^+-uncoordinated $TFSI^-$ and contact ion pairs, respectively. Compared with pristine PEO, two CPEs exhibit a higher proportion of free $TFSI^-$, indicating enhanced LiTFSI dissociation. Among them, MOF–NH_2 + PEO shows the highest Li^+-uncoordinated $TFSI^-$ content, consistent with the DFT results and confirming the strongest interaction between MOF–NH_2 and $TFSI^-$.

To clarify how the introduction of MOF and MOF–NH_2 influences the local coordination environment of Li^+ and $TFSI^-$ in PEO electrolyte, ^7Li and ^{19}F NMR were performed at 60 °C. The results provide insight into the ion dissociation behavior of these electrolytes. As shown in Fig. 3c and d, the pure PEO electrolyte exhibits broad, asymmetric peaks for both ^7Li and ^{19}F, indicative of a heterogeneous ion environment with significant ion pairing. Upon addition of MOF or MOF–NH_2, both signals narrow and converge to a single symmetric peak, suggesting enhanced salt dissociation and a more uniform Li^+ coordination environment.[50,51] The greater peak shift observed in the MOF–NH_2 + PEO compared to MOF + PEO further indicates that the –NH_2 introduces additional interactions with both Li^+ and $TFSI^-$.[52]

Together with the DFT and Raman results, the NMR analysis demonstrates that MOF–NH_2 effectively regulates the Li^+/$TFSI^-$ coordination structure, thereby providing a favorable environment for Li^+ transport within CPE.

The ionic conductivity of the electrolytes was measured by electrochemical EIS at various temperatures (Fig. 3e and f and Fig. S5 and Table S1). To determine the optimal filler content, composite polymer electrolytes containing 1–6 wt% MOF–NH_2 were first investigated. Among them, the electrolyte containing 2 wt% MOF–NH_2 exhibits the highest σ of 4.7×10^{-4} S cm^{-1} at 60 °C. Further increasing the filler content to 6 wt% results in a decrease in σ, which can be attributed to filler aggregation at high loadings and the resulting obstruction of Li^+ transport pathways. Therefore, 2 wt% MOF–NH_2 was selected as the optimal composition for subsequent studies. Using the optimized filler content, the σ of pristine PEO, MOF + PEO, and MOF–NH_2 + PEO was compared. The MOF–NH_2 + PEO exhibits the highest σ, which is substantially higher than those of pristine PEO (60 °C, 2.8×10^{-4} S cm^{-1}) and MOF + PEO (60 °C, 3.5×10^{-4} S cm^{-1}). To further quantify the influence of the fillers on the segmental dynamics of the PEO electrolyte, VTF fitting was conducted. VTF fitting yielded B = 2283, 2306, and 2320 for PEO, MOF + PEO, and MOF–NH_2 + PEO, respectively, with E_a = 0.197, 0.199, and 0.200 eV and $A = 5.19 \times 10^4$, 7.35×10^4, and 1.13×10^5 for the three electrolytes (Fig. S6). The nearly invariant E_a alongside the ~2.2-fold increase in A from PEO to MOF–NH_2 + PEO indicates that the enhanced conductivity arises mainly from an increased value of A rather than from changes in polymer segmental dynamics. This enhancement is consistent with the DFT, Raman, and NMR results, which indicate that the incorporation of MOF–NH_2 effectively regulates the Li^+/$TFSI^-$ coordination structure and promotes salt dissociation, thereby facilitating Li^+ transport within CPE. To further evaluate the influence of the fillers on Li^+ transport, the t_{Li^+} was measured at 60 °C using Li–Li symmetric cells *via* DC polarization combined with EIS (Fig. 3g–i). The MOF–NH_2 + PEO exhibits a higher t_{Li^+} value of 0.29, compared with 0.24 for MOF + PEO and 0.16 for PEO. The increased t_{Li^+} suggests that the incorporation of MOF-based fillers suppresses the contribution of anion migration to the overall ionic transport. Notably, the superior t_{Li^+} value of MOF–NH_2 + PEO further confirms the beneficial role of –NH_2 in strengthening the interaction with $TFSI^-$, which is in good agreement with the DFT calculations and Raman analysis.

The schematic illustration of the role of MOF fillers in regulating ion transport within the polymer electrolyte is proposed in Fig. 4a–c. Upon incorporation into the PEO electrolyte, the fillers interact with $TFSI^-$ and modify the local Li^+/$TFSI^-$ coordination structure. As shown in Fig. 4a, the incorporation of MOF–NH_2 into the PEO electrolyte induces the interaction between MOF–NH_2 and $TFSI^-$ and effectively regulates the local Li^+/$TFSI^-$ coordination structure, thereby releasing a large number of mobile Li^+. In comparison, fewer mobile Li^+ are observed in MOF + PEO (Fig. 4b) and pristine PEO (Fig. 4c). This enhanced anion electrostatic interaction in MOF–NH_2 + PEO facilitates LiTFSI dissociation, reduces Li^+-$TFSI^-$ ion pairing, and promotes Li^+ transport within PEO electrolyte. As a result, the MOF–NH_2 + PEO delivers the highest σ and t_{Li^+} among all samples. Nanoindentation measurements (Fig. S7a–c) show a slight decrease in hardness upon incorporation of the two fillers, suggesting that the improved electrochemical performance mainly originates from interfacial and

© 2026 The Author(s). Published by the Royal Society of Chemistry

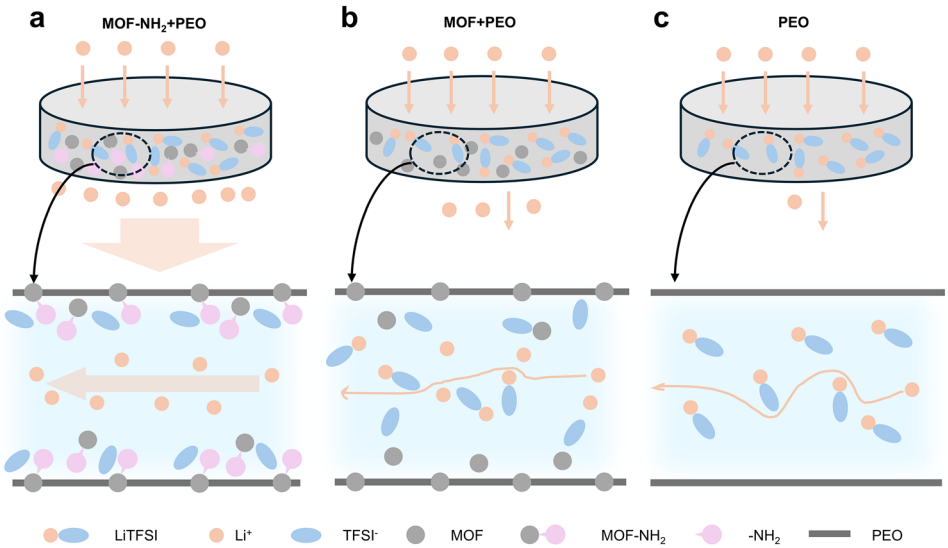


Fig. 4 Schematic diagram of the proposed Li^+ transport mechanism in (a) MOF–NH_2 + PEO, (b) MOF + PEO, and (c) pristine PEO electrolytes.

ion-transport regulation rather than mechanical reinforcement. Notably, black regions in Fig. S7b correspond to invalid indentation points where no reliable mechanical data could be obtained during the probe-based mapping measurement.

The electrochemical stability window of the electrolytes was evaluated at 60 °C by LSV, as shown in Fig. 5a. Among the samples, MOF–NH_2 + PEO exhibits the widest electrochemical window compared to PEO and MOF + PEO, indicating enhanced oxidative stability at high potentials. The improvement is likely associated with the interactions between MOF–NH_2 and the $TFSI^-$, which modifies the local chemical environment and contributes to improving electrolyte stability. It should be noted that since LSV is referenced against Li metal, a shift in the Li/Li^+ redox potential arising from changes in the Li^+ coordination environment cannot be completely excluded as a contributing factor.[53] Nonetheless, the observed widening of the electrochemical stability window suggests that MOF–NH_2 + PEO holds potential for improved compatibility with high-voltage cathode materials.

The interfacial stability toward Li metal was further evaluated using Li–Li symmetric cells with an electrolyte thickness of approximately 150 μm. As shown in Fig. 5b, the Li/MOF–NH_2 + PEO/Li cell exhibits highly stable Li plating/stripping over 1700 h at a current density of 0.1 mA cm^{-2} and a capacity limit of 0.1 mAh cm^{-2} at 60 °C. The initial polarization voltage is as low as 75 mV, which is lower than that of MOF + PEO (80 mV) and PEO (138 mV), indicating improved interfacial kinetics and more efficient Li^+ transport across the electrode/electrolyte interface. The polarization voltage of the PEO-based cell increases to 208 mV and exhibits severe fluctuations after 53 h, followed by a sudden voltage drop, suggesting internal short-circuiting likely caused by dendrite penetration. In contrast, the MOF–NH_2 + PEO based cell maintains stable voltage profiles without noticeable degradation. Such superior cycling stability indicates more uniform Li deposition and enhanced interfacial stability, which may be associated with the optimized ion-transport behavior of the electrolyte and the formation of a stable interphase on the Li surface. Further evidence is provided by the surface morphology of Li metal anode after 300 h cycling (Fig. S8a–c). A dense and smooth Li metal anode surface is observed for MOF–NH_2 + PEO, whereas uneven deposition with pits and grooves is found in PEO and MOF + PEO, which can induce local electric field amplification and accelerate dendrite growth.

To elucidate the origin of the enhanced interfacial stability in MOF–NH_2 + PEO, XPS was employed to analyse the composition of the SEI formed in Li–Li cells. The cells were cycled for 10 times at 0.1 mA cm^{-2} with a capacity limit of 0.1 mAh cm^{-2}.

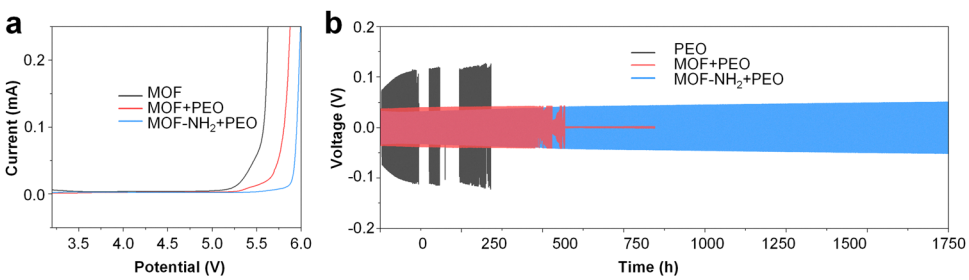


Fig. 5 (a) LSV of PEO, MOF + PEO and MOF–NH_2 + PEO. (b) Li plating/stripping cycling performance under 0.1 mA cm^{-2} constant current at 60 °C.

© 2026 The Author(s). Published by the Royal Society of Chemistry

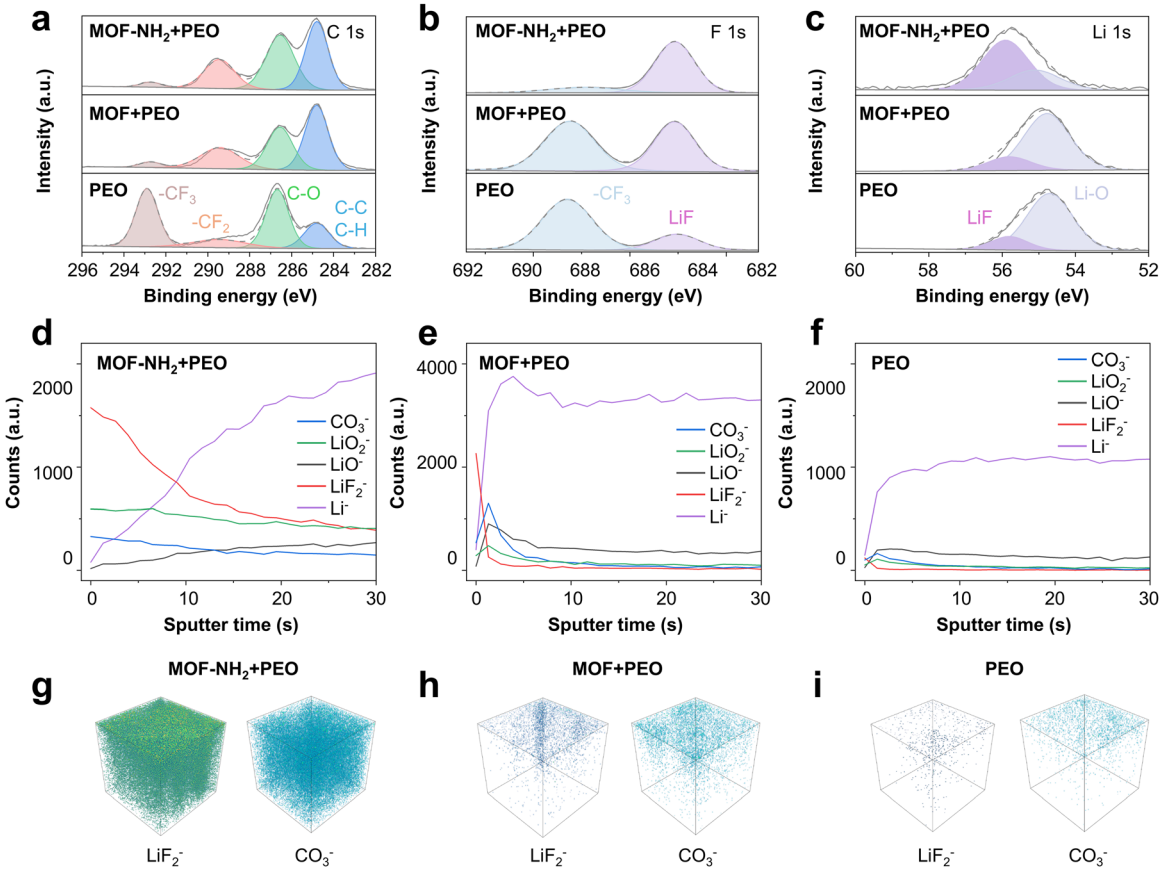


Fig. 6 (a)–(c) XPS spectra of c 1s, f 1s and Li 1s of MOF–NH_2 + PEO, MOF + PEO and PEO, respectively. (d)–(f) TOF-SIMS signal intensity analyses of Li metal surface after cycling with MOF–NH_2 + PEO, MOF + PEO and PEO, respectively. (g)–(i) 3d reconstructions of TOF-SIMS signals for sei (LIF^{2-} and CO^{3-}) on Li metal anode after cycling with MOF–NH_2 + PEO, MOF + PEO and PEO, respectively.

In the C 1s spectra (Fig. 6a), four components were identified: C–C/C–H (284.8 eV), C–O (286.5 eV), $-CF_2$ (289.5 eV), and $-CF_3$ (292.8 eV), corresponding to the PEO backbone and LiTFSI-derived species, respectively. The relative intensity of the C–C/C–H increased progressively from PEO to MOF + PEO to MOF–NH_2 + PEO, accompanied by a corresponding decrease in the C–O, suggesting degradation of the PEO ether backbone promoted by the MOF/MOF–NH_2. Upon incorporation of MOF and MOF–NH_2, the $-CF_3$ decreased while the $-CF_2$ increased, indicating enhanced decomposition of $TFSI^-$. This trend is corroborated by the F 1s spectra (Fig. 6b), where the relative intensity of the LiF (684.8 eV) increased markedly at the expense of the C–F (688.5 eV) in the MOF–NH_2 + PEO, suggesting accelerated $TFSI^-$ decomposition and LiF formation.[54] Consistently, the Li 1s spectra (Fig. 6c), deconvoluted into LiF (55.8 eV) and Li–O (54.7 eV), revealed an increase in the relative proportion of LiF from PEO to MOF + PEO to MOF–NH_2 + PEO. Taken together, these results demonstrate that the incorporation of MOF–NH_2 facilitates the formation of a LiF-rich SEI layer.

TOF-SIMS was further employed to investigate the spatial distribution of interfacial species of the disassembled Li metals in this study.[55–57] As shown in Fig. 6d–f, the LiF_2^- signal intensity in MOF–NH_2 + PEO is significantly higher than that in PEO and MOF + PEO. The 3D depth profiling (Fig. 6g–i) further provides evidence for the enhanced formation of LiF species, indicating the formation of a more uniform LiF-rich interphase. These results collectively demonstrate that MOF–NH_2 regulates interfacial chemistry by facilitating LiF-rich interphase formation. The resulting LiF-rich SEI contributes to improved interfacial stability, facilitated Li^+ transport, and improved interfacial ion transport.[58]

To evaluate the practical electrochemical performance of these electrolytes, Li–LFP full cells were assembled and tested at 60 °C and various current rates. The rate performance was first assessed at current rates ranging from 0.1 C to 2 C (Fig. 7a). The Li/MOF–NH_2 + PEO/LFP cell delivers stable reversible capacities of 168.9, 168.9, 166.1, 158.8, 148.5, and 136.9 mAh g^{-1} at 0.1, 0.2, 0.5, 1, 1.5, and 2C, respectively at 60 °C. Even at a high rate of 2C, a capacity of 136.9 mAh g^{-1} is maintained, corresponding to approximately 81% of the capacity obtained at 0.1C. When the current rate is returned to 0.5 C, the discharge capacity rapidly recovers to 165.5 mAh g^{-1} and remains stable, demonstrating excellent reversibility and structural stability during repeated rate variations. In contrast, the cell based on pristine PEO exhibits severe capacity deterioration with increasing current density and delivers only ~50 mAh g^{-1} at 2C. The corresponding charge–discharge profiles (Fig. 7b–d) show that both MOF-containing electrolytes exhibit substantially lower voltage

© 2026 The Author(s). Published by the Royal Society of Chemistry

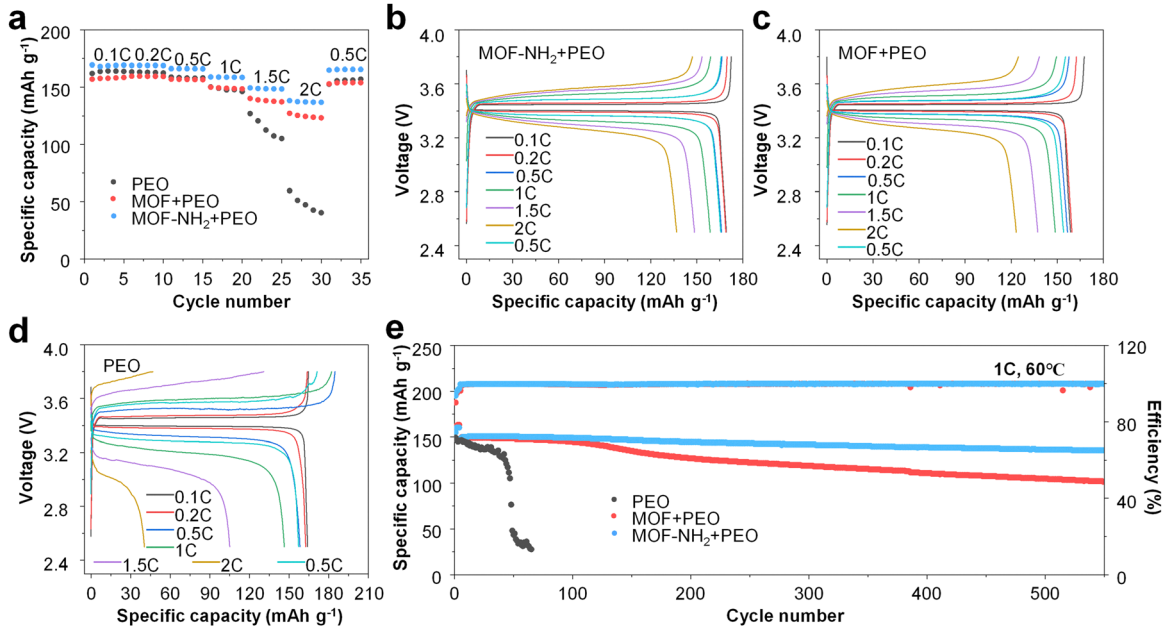


Fig. 7 (a) The rate performance of Li–LFP cells with MOF–NH_2 + PEO, MOF + PEO and PEO at 60 °C. (b)–(d) Charge–discharge curves corresponding to the rate performance (the fifth cycle at each rate) of the Li–LFP cells with MOF–NH_2 + PEO, MOF + PEO and PEO respectively. (e) Long-term cycling performance of Li–LFP cells with MOF–NH_2 + PEO, MOF + PEO and PEO at 1C rate and 60 °C.

polarization than pristine PEO, indicating improved electrochemical kinetics during cell operation. Notably, the MOF–NH_2 + PEO cell consistently delivers higher capacities than the MOF + PEO cell, particularly at elevated current rates, highlighting the beneficial role of amino-functionalized MOF fillers in supporting fast and stable Li^+ transport.

Long-term cycling performance was further evaluated at 1 C and 60 °C (Fig. 7e). The Li/MOF–NH_2 + PEO/LFP cell exhibits outstanding cycling stability, retaining 90.5% of its initial capacity after 550 cycles. In comparison, the discharge capacity of the PEO-based cell rapidly decreases to 27.6 mAh g^{-1} within only 60 cycles, while the MOF + PEO cell retains only 60% of its initial capacity after 550 cycles. The results of rate performance and long cycle performance indicate that MOF–NH_2 contributes significantly to the excellent cycle stability of the ASSLB. The electrochemical performance of MOF–NH_2 + PEO was compared with other works on PEO-based electrolytes (Table S2).

To evaluate the solid-state electrolyte/cathode interfacial chemistry, TOF-SIMS depth profiling was conducted on the

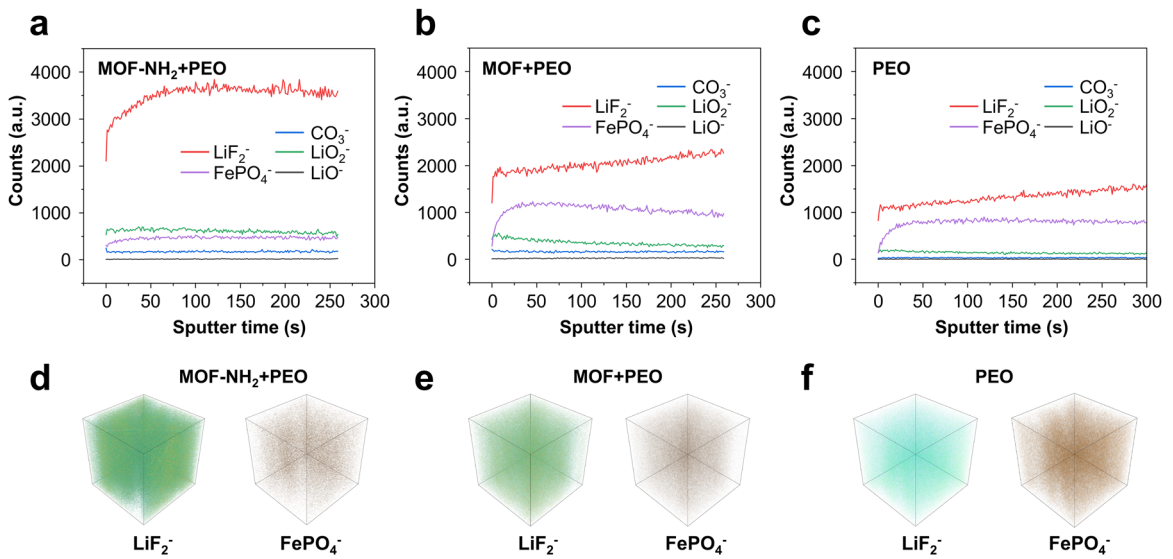


Fig. 8 (a)–(c) TOF-SIMS signal intensity analyses of $LIFePO_4$ cathode surface after cycling with MOF–NH_2 + PEO, MOF + PEO and PEO, respectively. (d)–(f) 3d reconstructions of TOF-SIMS signals for LiF_2^-, $FePO_4^-$ after cycling with MOF–NH_2 + PEO, MOF + PEO and PEO, respectively.

© 2026 The Author(s). Published by the Royal Society of Chemistry

cycled LFP electrodes (8 cycles; 0.5 C; discharged state) to analyse the CEI. As illustrated in Fig. 8a–c, the evolution of the characteristic inorganic CEI fragment (LiF_2^-) and the bulk LFP substrate fragment ($FePO_4^-$) was analysed. The relative evolution of LiF_2^- and $FePO_4^-$ provides information regarding the fluorinated character and surface coverage of the CEI. As illustrated in Fig. 8a, the MOF–NH_2 + PEO exhibits a dominant LiF_2^- signal along with a low substrate-derived $FePO_4^-$ intensity, achieving a substantially high $LiF_2^-/FePO_4^-$ ratio of > 7.0. Such behavior suggests the formation of a fluorine-rich interphase that effectively covers the LFP surface. In comparison, with the addition of MOF (Fig. 8b), the ratio is decreased to $\sim$2.0. For the pure PEO (Fig. 8c), the $LiF_2^-/FePO_4^-$ ratio is $\sim$1.5. This implies that MOF + PEO and PEO have a smaller effect on the decomposition of LiTFSI than MOF–NH_2. This contrast is further authenticated by the 3D reconstructions (Fig. 8d–f). Compared with MOF + PEO and pristine PEO, the MOF–NH_2 + PEO exhibits the strongest LiF_2^- distribution across the cathode surface. Such behavior is particularly evident for the MOF–NH_2 + PEO electrolyte, implying more extensive formation and distribution of LiF-containing interphase.

4. Conclusions

In summary, two structurally analogous one-dimensional MOF fillers, MOF and MOF–NH_2, were employed as model fillers to elucidate the role of amino functionalization in PEO-based electrolyte. Owing to the strong interaction between the –NH_2 and $TFSI^-$, MOF–NH_2 facilitates LiTFSI dissociation and increases the concentration of mobile Li^+, leading to enhanced ionic conductivity and a higher Li-ion transference number. Meanwhile, the altered $TFSI^-$ chemistry also affects the interfacial reactions at both the Li metal anode and LFP cathode interfaces, promoting the formation of LiF-rich interphases with improved interfacial stability. As a result, the MOF–NH_2 enables highly stable Li plating/stripping for over 1700 h and delivers excellent electrochemical performance in Li/LFP cells, retaining 90.5% of its initial capacity after 550 cycles at 1C and 60 °C. Through the direct comparison between MOF and MOF–NH_2, this work reveals the critical role of amino functionalization in regulating $TFSI^-$ chemistry. More importantly, the results demonstrate that tailoring filler–anion interactions is an effective strategy for simultaneously optimizing ionic transport and interfacial stability, providing new insights into the rational design of high-performance CPEs for ASSLBs.

Author contributions

Sihao Xing: writing – review & editing, visualization, validation, investigation, and data curation. Gen Hasegawa: NMR analysis, writing – review & editing. Prince Sharma: review & editing. Marcela Calpa: assisted in testing electrochemical cycles, review & editing. Denis Y. W. Yu: assisted in testing electrochemical cycles, review & editing. Takuya Masuda: assisted in testing nanoindentation, review & editing. Kazunori Takada: funding acquisition and review & editing. Naoaki Kuwata: supervision, conceptualization, funding acquisition and review & editing.

Conflicts of interest

There are no conflicts of interest to declare.

Data availability

All data supporting the research in this paper are available in the main text and supplementary information (SI). The supplementary information includes Fig. S1–S8 and Tables S1–S2. See DOI: https://doi.org/10.1039/d6ma01112h.

Acknowledgements

This study was supported by JST GteX Program, Grant Number JPMJGX23S2 and NIMS All-Solid-State Battery Materials Open Platform (MOP). This study is also supported by MEXT Materials Processing Science project (''Materealize'') Grant Number JPMXP0219207397, JST COI-NEXT ''Center for Advanced Battery Collaboration'' Grant Number JPMJPF2016, JSPS KAKENHI Grant Number 24H02205 (Ion Jamology). The TOF-SIMS, FIB, SEM, and EDS measurements were supported by the NIMS technical support (NIMS Battery Research Platform).

References

1 K. J. Harry, D. T. Hallinan, D. Y. Parkinson, A. A. Macdowell and N. P. Balsara, *Nat. Mater.*, 2014, **13**, 69–73.
2 J. M. Tarascon and M. Armand, *Nature*, 2001, **414**, 359–367.
3 A. Zhamu, G. Chen, C. Liu, D. Neff, Q. Fang, Z. Yu, W. Xiong, Y. Wang, X. Wang and B. Z. Jang, *Energy Environ. Sci.*, 2012, **5**, 5701–5707.
4 T. Famprikis, P. Canepa, J. A. Dawson, M. Saiful Islam and C. Masquelier, *Nat. Mater.*, 2019, **18**, 1278–1291.
5 X. B. Cheng, C. Z. Zhao, Y. X. Yao, H. Liu and Q. Zhang, *Chem*, 2019, **5**, 74–96.
6 A. Manthiram, X. Yu and S. Wang, *Nat. Rev. Mater.*, 2017, **2**, 16103.
7 L. Long, S. Wang, M. Xiao and Y. Meng, *J. Mater. Chem. A*, 2016, **4**, 10038–10069.
8 D. Zhou, D. Shanmukaraj, A. Tkacheva, M. Armand and G. Wang, *Chem*, 2019, **5**, 2326–2352.
9 C. Sun, J. Liu, Y. Gong, D. P. Wilkinson and J. Zhang, *Nano Energy*, 2017, **33**, 363–386.
10 S. Liu, W. Liu, D. Ba, Y. Zhao, Y. Ye, Y. Li and J. Liu, *Adv. Mater.*, 2023, **35**, e2110423.
11 Z. Xue, D. He and X. Xie, *J. Mater. Chem. A*, 2015, **3**, 19218–19253.
12 R. Chang, Y. Liu, Y. Zhang, Y. Shi, J. Tang, Z. L. Xu, X. Zhou and J. Yang, *Adv. Energy Mater.*, 2025, **15**, 2405906.

© 2026 The Author(s). Published by the Royal Society of Chemistry

13 Y. Zhang, H. Gao, J. Wang, Q. Chi, T. Zhang, C. Zhang, Y. Feng, Y. Zhang, D. Cao and K. Zhu, *Inorg. Chem. Front.*, 2024, **4**, 1289–1300.
14 K. Nie, X. Wang, J. Qiu, Y. Wang, Q. Yang, J. Xu, X. Yu, H. Li, X. Huang and L. Chen, *ACS Energy Lett.*, 2020, **5**, 826–832.
15 L. Yang, D. Luo, Y. Zheng, T. Yang, Q. Ma, Y. Nie, H. Dou, Y. Zhang, R. Huang, A. Yu, L. Shui, X. Wang and Z. Chen, *Adv. Funct. Mater.*, 2022, **32**, 2204778.
16 X. Su, X. P. Xu, Z. Q. Ji, J. Wu, F. Ma and L. Z. Fan, *Electrochem. Energy Rev.*, 2024, **7**, 2.
17 R. Li, H. Hua, X. Yang, J. Tian, Q. Chen, R. Huang, X. Li, P. Zhang and J. Zhao, *Energy Environ. Sci.*, 2024, **17**, 5601–5612.
18 X. Song, K. Ma, J. Wang, H. Wang, H. Xie, Z. Zheng and J. Zhang, *ACS Nano*, 2024, **18**, 12311–12324.
19 X. Yang, M. Jiang, X. Gao, D. Bao, Q. Sun, N. Holmes, H. Duan, S. Mukherjee, K. Adair, C. Zhao, J. Liang, W. Li, J. Li, Y. Liu, H. Huang, L. Zhang, S. Lu, Q. Lu, R. Li, C. V. Singh and X. Sun, *Energy Environ. Sci.*, 2020, **13**, 1318–1325.
20 Y. Wei, T. H. Liu, W. Zhou, H. Cheng, X. Liu, J. Kong, Y. Shen, H. Xu and Y. Huang, *Adv. Energy Mater.*, 2023, **13**, 2203547.
21 Y. Su, F. Xu, X. Zhang, Y. Qiu and H. Wang, *Nano-Micro Lett.*, 2023, **15**, 82.
22 H. Zhai, P. Xu, M. Ning, Q. Cheng, J. Mandal and Y. Yang, *Nano Lett.*, 2017, **17**, 3182–3187.
23 X. Yu and A. Manthiram, *Energy Storage Mater.*, 2021, **34**, 282–300.
24 N. Wu, P. H. Chien, Y. Qian, Y. Li, H. Xu, N. S. Grundish, B. Xu, H. Jin, Y. Y. Hu, G. Yu and J. B. Goodenough, *Angew. Chem., Int. Ed.*, 2020, **59**, 4131–4137.
25 X. Tao, Y. Liu, W. Liu, G. Zhou, J. Zhao, D. Lin, C. Zu, O. Sheng, W. Zhang, H. W. Lee and Y. Cui, *Nano Lett.*, 2017, **17**, 2967–2972.
26 J. E. Weston and B. C. H. Steele, *Solid State Ionics*, 1982, **7**, 75–79.
27 C. Capiglia, P. Mustarelli, E. Quartarone, C. Tomasi and A. Magistris, *Solid State Ionics*, 1999, **118**, 73–79.
28 J. Zheng and Y. Y. Hu, *ACS Appl. Mater. Interfaces*, 2018, **10**, 4113–4120.
29 S. Dong, Y. Zheng, Q. Duan, Y. Zhao, T. Tan, Y. Zhou, T. Rao, H. Yan, W. Guo and D. Y. W. Yu, *J. Mater. Chem. A*, 2025, **13**, 9453–9461.
30 Z. Li, W. Zhang, Y. Chen, Q. Lin, L. Zhang, J. Tao, O. V. Kolosov, J. Li, Y. Lin and Z. Huang, *J. Mater. Sci. Technol.*, 2024, **183**, 184–192.
31 Z. Qian, Z. Qiu, R. Wang, M. Wei, A. Fei, Z. Hu, H. Mohamed, L. Chen, Y. Li and B. Su, *Chem. Eng. J.*, 2025, **514**, 163121.
32 Y. Wang, X. Chen, W. Zhao, Q. Yu, Q. Zhang, Y. Zhou, J. Liu, X. Xing and Y. Zhang, *J. Phys. Chem. C*, 2025, **129**, 4333–4344.
33 S. Wu, X. Li, C. Qi, L. Liu, X. Ke, R. Xu, X. Fu and C. Lei, *J. Mater. Sci.*, 2025, **60**, 21357–21370.
34 C. Gong, Z. He, Q. Chen, W. Xu and B. Cheng, *Chem. Eng. J.*, 2026, **538**, 176838.
35 L. Dai, M. Cai, X. Zhou, W. Liang, Z. Zhao, Z. Xia, F. Huang, J. Jiang, W. Jiang, B. Zhang and Z. Ma, *Chem. Sci.*, 2025, **16**, 2453–2464.
36 Q. Hao, J. Yan, Y. Gao, F. Chen, X. Chen, Y. Qi and N. Li, *ACS Appl. Mater. Interfaces*, 2024, **16**, 44689–44696.
37 C. Wang, S. Xiang, L. Chen, L. Liang, J. Tu, S. Shen, H. Cao and H. Zhang, *Adv. Mater.*, 2025, **38**, e16702.
38 X. Xu, Y. Fang, L. Lin, Z. S. Wu, Y. Xia, D. Ruan, P. Jiang and Y. Cao, *J. Power Sources*, 2025, **650**, 237504.
39 P. Yang, Z. Wen, Y. Jia, J. Wang, X. Ding and Y. Xu, *Adv. Funct. Mater.*, 2026, **36**, e75367.
40 M. Yang and T. H. Epps, *Macromolecules*, 2026, **59**, 5005–5016.
41 T. Ma, B. Fu, H. Feng, Y. Li, Y. Zhai, Y. Tian, Z. Li and Z. M. Su, *Angew. Chem., Int. Ed.*, 2025, **64**, e202501412.
42 K. Yuan, Z. Liu, Z. Yan, Q. Yun, T. Song, J. Guo, X. Zhang, D. Zhong, Z. Tang, T. Lu and W. Hu, *Angew. Chem., Int. Ed.*, 2024, **63**, e202402693.
43 M. Zhang, R. Tan, M. Wang, Z. Zhang, C. T. John Low and Y. Lai, *Battery Energy*, 2024, **3**, 20230050.
44 T. Wei, Q. Zhang, S. Wang, M. Wang, Y. Liu, C. Sun, Y. Zhou, Q. Huang, X. Qiu and F. Tian, *Int. J. Miner., Metall. Mater.*, 2023, **30**, 1897–1905.
45 T. W. Quadri, E. D. Akpan, S. E. Elugoke, O. Dagdag, N. J. Nnaji, C. Verma, L. O. Olasunkanmi, A. AlFantazi, V. C. Anadebe and R. C. Barik, *et al.*, *Coord. Chem. Rev.*, 2025, **523**, 216285.
46 C. Kang, J. Zhu, Y. Wang, S. Ye, Y. Xiong, F. Kong and G. Yin, *Energy Storage Mater.*, 2023, **61**, 102898.
47 S. I. Noro, X. Zheng, A. Q. Wang, K. Suzuki, S. Kosasang, S. Horike, D. Padovan, K. Nakajima, H. Sato, K. Takahashi and T. Nakamura, *Inorg. Chem.*, 2022, **61**, 3379–3386.
48 S. I. Noro, Y. Meng, K. Suzuki, M. Sugiura, Y. Hijikata, J. Pirillo, X. Zheng, K. Takahashi and T. Nakamura, *Inorg. Chem.*, 2021, **60**, 4531–4538.
49 G. M. Barca, C. Bertoni, L. Carrington, D. Datta, N. De Silva, J. E. Deustua, D. G. Fedorov, J. R. Gour, A. O. Gunina and E. Guidez, *et al.*, *J. Chem. Phys.*, 2020, **152**, 154102.
50 C. D. Fang, Y. Huang, Y. F. Sun, P. F. Sun, K. Li, S. Y. Yao, M. Y. Zhang, W. H. Fang and J. J. Chen, *Nat. Commun.*, 2024, **15**, 6781.
51 Y. Zhu, W. Deng, Y. Tan, J. Shi, J. Wu, W. Lu, J. Jia, S. Wang and Y. Zou, *Adv. Funct. Mater.*, 2023, **33**, 2304985.
52 J. Peng, Y. Xiao, D. A. Clarkson, S. G. Greenbaum, T. A. Zawodzinski and X. C. Chen, *ACS Appl. Polym. Mater.*, 2020, **2**, 1180–1189.
53 S. Ko, T. Obukata, T. Shimada, N. Takenaka, M. Nakayama, A. Yamada and Y. Yamada, *Nat. Energy*, 2022, **7**, 1217–1224.
54 D. Qu, T. Liu, Y. Sun, Y. Yan, C. Li, Z. Cui, C. Gao, S. Kong, Z. Zhang and Z. Liu, *et al.*, *Adv. Mater.*, 2025, **37**, e05762.
55 N. Kuwata, G. Hasegawa, D. Maeda, N. Ishigaki, T. Miyazaki and J. Kawamura, *J. Phys. Chem. C*, 2020, **124**, 22981–22992.
56 G. Hasegawa, N. Kuwata, T. Ohnishi and K. Takada, *J. Mater. Chem. A*, 2024, **12**, 731–738.
57 S. Xing, G. Hasegawa, P. Sharma, D. Ito, K. Kamiguchi, K. Takada and N. Kuwata, *ACS Energy Lett.*, 2026, **11**, 1889–1896.
58 Y. Liu, X. Tao, Y. Wang, C. Jiang, C. Ma, O. Sheng, G. Lu and X. Luo, *Science*, 2022, **375**, 739–745.

© 2026 The Author(s). Published by the Royal Society of Chemistry